Bulletin of the Seismological Society of America, Vol. 104, No. 6, pp. 2933–2942, December 2014, doi: 10.1785/0120140109

Rupture Directivity Effect and Stress Heterogeneity of the 2013 Nantou Blind-Thrust Earthquakes, Taiwan

by Yi-Ying Wen, Hiroe Miyake, Yin-Tung Yen, Kojiro Irikura, and Kuo-En Ching

Abstract We investigated broadband evidence of the rupture directivity effect and estimated stress drop for the 2013 Nantou blind-thrust earthquakes (the 0327 and 0602 crustal events) from three individual analyses using empirical Green's functions: deconvolution source time function analysis, source spectral ratio analysis, and broadband waveform modeling of a strong-motion generation area. Although these two adjacent events have similar focal mechanisms, the 0327 event shows only up-dip directivity to the west, with an estimated stress drop of 9.0 MPa, and the 0602 event displays significant rupture directivity to the southwest, with an estimated stress drop of 14.2 MPa. The obvious variance in the rupture behavior and stress drop of these two nearby events, which might be related to immature blind faulting, suggests that this region requires additional study of the stress heterogeneity to better assess the seismic hazard.

Introduction

Two moderate-sized crustal earthquakes, which occurred on 27 March 2013 (named the 0327 event, with M_L 6.2) and 2 June 2013 (named the 0602 event, with M_L 6.5), struck the Nantou area in the central part of Taiwan (Fig. 1a, Table 1). According to the reports of the Central Geological Survey (2013a,b), these two events were both motivated by east-dipping thrust movement of blind faults, which are not related to the surrounding active faults such as the Chelungpu and Tamaopu-Shuangtung faults. This is also supported by the aftershock distribution (Fig. 1b,c). The geodetic fault inversion of Chuang *et al.* (2013) also suggested east-dipping reverse-slip models for both events. The inversion indicates the events occurred on a deep extension of a mature shallow fault or a newly developed deep ramp fault, with respect to a crustal-thickening model (Wu *et al.*, 2004). In addition, Central Geological Survey (2013a,b) revealed that these two events caused some damage and casualties due to the strong ground shaking in the northwest to west-northwest region of the 0327 event and in the southwest to west-southwest region of the 0602 event, respectively.

Almost 100 years ago, the Nantou area was also seriously damaged by the 1916 Nantou earthquake sequence ($5.5 \leq M_L \leq 6.8$, Cheng *et al.*, 1999), as shown in Figure 1b. It was a coincidence that the 2013 Nantou earthquakes showed some similarities to the 1916 Nantou earthquake sequence: (1) there was an interval of tens of days between events, (2) the events magnitudes were larger than five, and (3) the events locations were very close. Furthermore, several events with $M_w \geq 6.0$ occurred around this region after the 1999 M_w 7.6 Chi-Chi earthquake. To estimate the potential seismic hazard to the Nantou area, it is crucial to investigate the detailed source characteristics of the 2013 Nantou earthquakes. In this study, using small-event records as the empirical Green's functions (EGFs), we performed three individual types of source analyses in the broadband period range, that is, we (1) derived the directivity effect from relative source time functions using regional broadband waveforms, (2) validated the rupture directivity from source spectral ratios, and (3) estimated the strong-motion generation area (SMGA) and stress drop by fitting the synthetics to the observed ground-motion records. These overall broadband analyses are quite effective for better understanding the source characteristics, especially in the shorter-period range, which is integral for seismic-hazard assessment.

Data and Methodology

To retrieve the primary rupture characteristics of an earthquake and to introduce minimal *a priori* assumptions for the available seismic data, different approaches using small-event records as EGFs have been well developed and frequently applied to study the source properties of earthquakes (e.g., Irikura, 1986; Irikura and Kamae, 1994; Velasco *et al.*, 1994; Lay and Wallace, 1995). For the criteria of the EGFs, a smaller event (typically 1–2 magnitude units smaller than the mainshock) with a similar focal mechanism and close hypocenter location relative to the mainshock is used (Velasco *et al.*, 1994; Lay and Wallace, 1995). Considering the similar focal mechanisms and close locations of the two 2013 Nantou earthquakes and the data quality of the smaller events, we selected the 26 June 2011 M_L 5.0 event (Fig. 1a, Table 1) as an EGF. The epicenters and fault-plane solutions of the two 2013 Nantou earthquakes and the EGF were determined by the Central Weather Bureau (CWB) and the Broadband Array in Taiwan for Seismology (BATS), respectively (Table 1). We applied three approaches using various seismic waveform data,

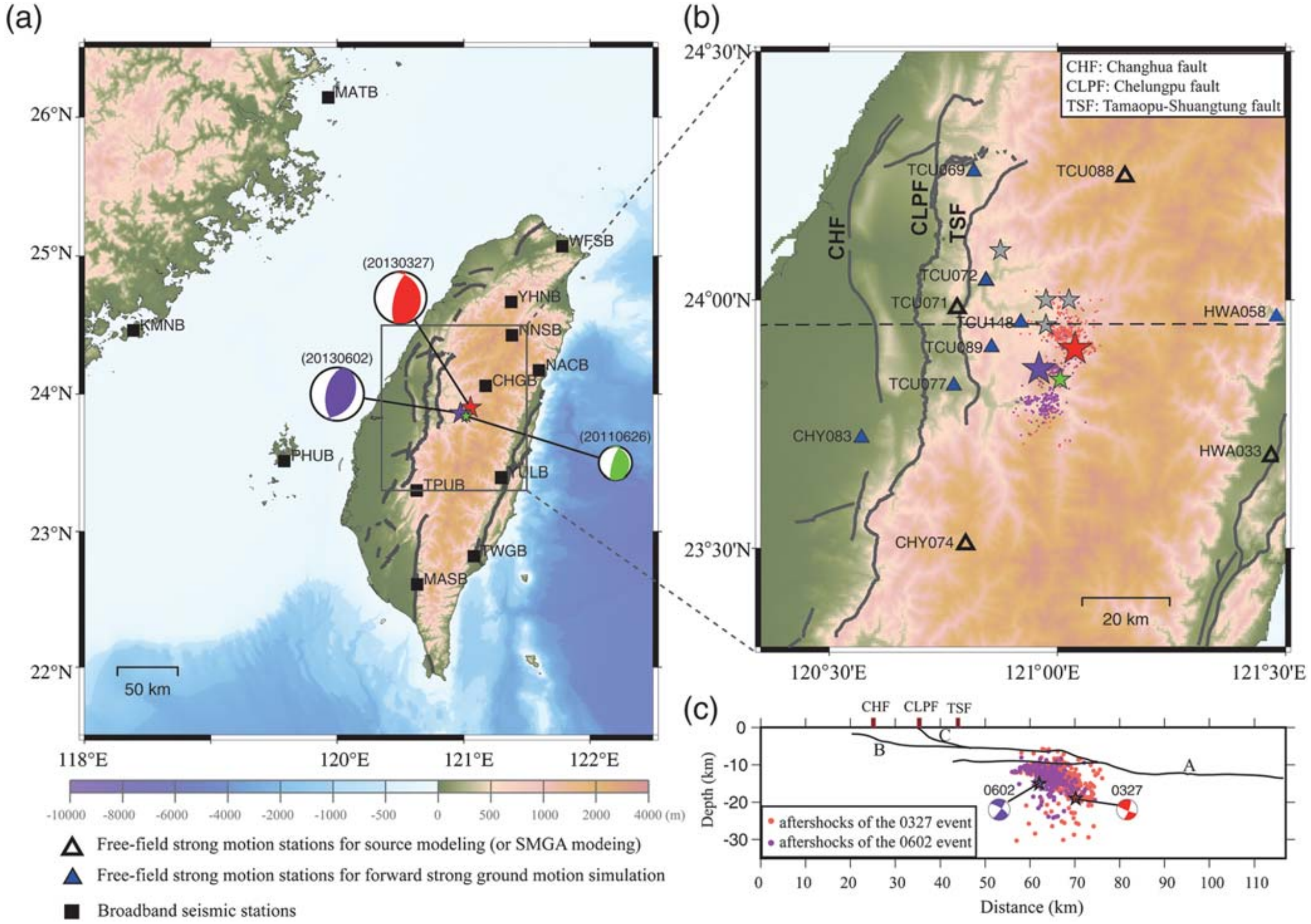

Figure 1. (a) Epicenters (stars) and focal mechanisms for the 2013 Nantou earthquakes and the EGF event listed in Table 1 and the broadband seismic stations (squares) that are utilized in the deconvolution analysis. (b) Free-field strong-motion stations used in the source spectral ratio analysis and the EGF simulation. Magenta and purple dots denote the aftershocks of the 0327 and 0602 events within 15 days, recorded by CWB, respectively. The gray stars show the epicenters of the 1916 Nantou earthquake sequence. (c) Cross section of aftershocks and focal mechanisms of the 2013 Nantou earthquakes. Faults A, B, and C represent the Taiwan main detachment (Carena *et al.*, 2002), the shallow Chinshui detachment (Yue *et al.*, 2005), and the Chelungpu fault, respectively. The active faults (thick gray lines) identified by Central Geological Survey of Taiwan are also shown.

including deconvolution analysis with the broadband seismic data in the time domain, source spectral ratio analysis in the frequency domain, and broadband ground-motion simulation with near-source ground-motion data in the time domain. Three methods are described in detail in the following sections.

Deconvolution Analysis to Estimate Source Time Functions

Deconvolution analysis using EGF is a well-known technique and has been successfully applied to studies on source process and rupture directivity effect (e.g., Velasco *et al.*, 1994; Ammon *et al.*, 2005; Wen *et al.*, 2012; Orefice *et al.*, 2013). Because both of the 2013 Nantou earthquakes caused strong ground shaking in the central and western regions of Taiwan, our first step was to examine the directivity effect from the source time functions of these two events. We used broadband seismic data from 12 strong-motion stations (Fig. 1a) that were provided by BATS; the data have good azimuthal coverage and feature high-quality recordings of both the mainshocks and the EGF event. For the original mainshock and the EGF *P*-wave seismograms, we removed the instrument response, integrated the records into displacement, and bandpass filtered the data from 0.1 to 2 Hz. We used the filtered displacement waveforms to obtain the relative source time functions through an iterative time-domain deconvolution procedure (Kikuchi and Kanamori, 1982) with a positivity constraint in the algorithm (Chu *et al.*, 2009). The derived source time functions for the 0327 and 0602 events are shown in Figure 2.

Source Spectral Ratio Analysis to Investigate Rupture Directivity

Miyake *et al.* (1999) proposed a source spectral ratio fitting approach by fitting the observed source spectral ratio between the mainshock and EGF event to that of a theoretical source. Based on the omega-squared source model of Brune (1970, 1971), the theoretical source spectral ratio function can be represented as

Table 1

Earthquake Parameters for the 2013 Nantou Earthquakes and the EGF Event

	2011/06/26 (EGF Event)	2013/03/27 (0327 Event)	2013/06/02 (0602 Event)
Epicenter	121.00° E 23.85° N	121.05° E 23.90° N	120.97° E 23.86° N
Depth (km)	14.8	19.4	14.5
Fault plane (strike/dip/rake)	335/19/50	344/23/62	30/37/106
M_L	5.0	6.2	6.5

The epicenters and fault-plane solutions were determined by the Central Weather Bureau (CWB) and Broadband Array in Taiwan for Seismology (BATS), respectively.

$$\mathrm{SSRF}(f) = \frac{M_0}{m_0}\frac{1+(f/f_{\mathrm{ca}})^2}{1+(f/f_{\mathrm{cm}})^2}, \qquad (1)$$

in which M_0/m_0 corresponds to the seismic moment ratio between the mainshock and EGF event at the lowest frequency, and f_{cm} and f_{ca} represent the corner frequencies of the mainshock and the EGF event, respectively. Following Irikura (1986), the scaling parameters N and C, which are the ratios of the fault dimensions and stress drop between the mainshock and the EGF event, respectively, can be derived from the constant levels of the acceleration and displacement spectra of the mainshock and EGF event using the formulas

$$U_0/u_0 = M_0/m_0 = CN^3, \qquad A_0/a_0 = CN, \qquad (2)$$

Here, U_0 and u_0 indicate the flat levels of the displacement spectra of the mainshock and the EGF event, respectively. A_0 and a_0 are the flat levels of the acceleration spectra of the mainshock and the EGF event, respectively. The fault area of mainshock can be divided into $N \times N$ subfaults with sizes equivalent to the rupture area of EGF event. Using the weighted least-squares method of Miyake *et al.* (1999, 2003), the above parameters can be estimated through fitting the observed source amplitude spectral ratio to the theoretical source spectral ratio function. To observe the low-frequency spectral variations, which are affected by the rupture directivity effect (Miyake *et al.*, 2001), data from four stations (open triangles in Fig. 1b) were used to obtain the source spectral ratios for the mainshock to the EGF event after canceling out the effects of propagation path and site amplification. The period range is 0.2–10 Hz, and the vector summation of the three-component amplitude spectra was calculated for a 30-s waveform duration, which included the entire *S* waves. Then, the mean observed source spectral ratio was used to derive the parameters N and C.

Empirical Green's Function Simulation to Estimate SMGA and Stress Drop

A heterogeneous slip model has been successfully derived by deterministic waveform inversion up to ~1 Hz based on near-source ground-motion data. However, the frequency range of 0.5–2.0 Hz is important and interesting for most earthquake engineering applications. The SMGA, which reproduces the near-source strong ground motions in the frequency range up to ~10 Hz, can be defined as the characteristic area with a uniform and high slip velocity in the total rupture area; this area occupied almost the same area of the asperity (large slip region, which can usually be identified by waveform inversion) (Miyake *et al.*, 2001, 2003). In this study, we used the EGF method developed by Irikura (1986) and Irikura and Kamae (1994) to estimate the SMGA of the 0327 and 0602 events by simulating the acceleration, velocity, and displacement waveforms in a frequency range of 0.2–10 Hz for the stations surrounding the source area. We used free-field strong-motion data maintained by CWB; 11 stations (Fig. 1b) were selected based on the locations of the mainshocks and the EGF event near the Central Range.

To avoid spectral shape distortion due to the rupture directivity effect, we chose four stations (open triangles in Fig. 1b) for the source spectral ratio fitting procedure (as described in the above section). We allowed the rupture velocity to be 0.7–0.95 times the *S*-wave velocity (V_S), based on the 3D velocity model (Kuo-Chen *et al.*, 2012). Because we used the same event as the EGF for the two 2013 Nantou earthquakes, the rupture area and the rise time of the EGF should be the same. After performing a grid search to find the optimal waveform fit, we obtained the parameters related to the SMGA, such as the initiation position (rupture starting point), the size of the SMGA, the rupture velocity, and the rise time, as listed in Table 2. We also applied the forward modeling to the other stations (blue solid triangles in Fig. 1b) to validate the applicability of the SMGA model.

We further estimated the stress drop of the two Nantou earthquakes from the SMGA and the seismic moment obtained by the Global Centroid Moment Tensor (CMT) solution (Madariaga, 1979; Boatwright, 1988; Miyake *et al.*, 2003):

$$\Delta\sigma = \frac{7}{16}\frac{M_0}{Rr^2}, \qquad (3)$$

in which R is the equivalent radius for the total rupture area $S(S = \pi R^2)$. We estimated S and the characterized asperity S_{ASP} from the inversion model of Chuang *et al.* (2013) according to the trimming criteria of Somerville *et al.* (1999). r represents the equivalent radius for SMGA, or the characterized asperity ($\mathrm{SMGA} = \pi r^2$ or $S_{\mathrm{ASP}} = \pi r^2$).

Results

Figure 2a,b shows the retrieved relative source time functions of the 0327 and 0602 events, respectively. The stations on the west side (e.g., KMNB and PHUB) yielded the largest amplitudes of the source time function for both events.

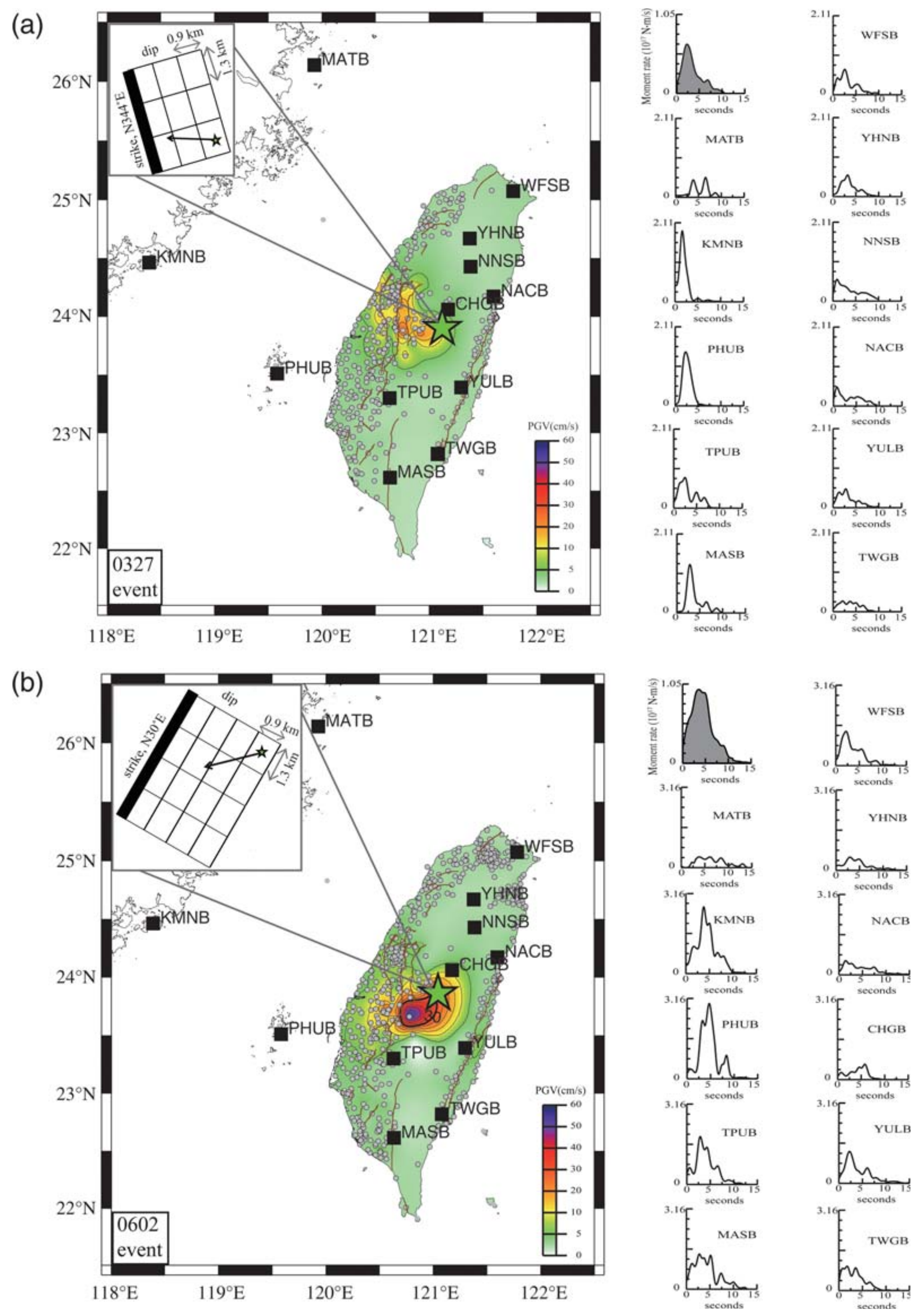

Figure 2. The observed peak ground velocity distribution determined from free-field strong-motion stations (circles), relative source time functions (black lines), and average source time function (gray shadow) of the (a) 0327 and (b) 0602 events, respectively. Stars show epicenters of the mainshocks, and squares represent broadband seismic stations. The inset shows the schematic of the slip direction (black vector) and the rupture starting point (star) on the strong-motion generation area (SMGA).

The up-dip rupture directivity along the fault plane toward the west is consistent with the faulting mechanism inverted by the geodetic data (Chuang *et al.*, 2013). For the 0327 event, except for stations KMNB and PHUB, the relative source time functions of other stations show similar amplitudes, suggesting that the main feature of the rupture directivity is related to up-dip slip direction but not the strike direction. For the 0602 event, the amplitudes of the relative source time functions for the stations to the southwest (e.g., PHUB and TPUB) are obviously higher than those for the stations located to the northeast (e.g., NACB and CHGB). It indicates the directivity effect with rupture propagating to the southwest for the 0602 event. The rupture patterns of the two 2013 Nantou earthquakes are consistent with the coseismic slip models derived by Chuang *et al.* (2013). In addition, the observed peak ground velocity distributions, as shown in Figure 2a,b, seems to support the results of the deconvolution analysis, which suggests the high peak ground velocity was concentrated near the west region of the epicenter during the faulting of the 0327 event but displayed a trend to the southwest for the 0602 event.

Usually, measurements at stations located in the direction of forward rupture exhibit high corner frequency (e.g., Boore and Joyner, 1978) and steep source spectral decay (e.g., Miyake *et al.*, 2001) compared with the omega-squared source spectral model (Brune, 1970). Conversely, measurements at stations located in the direction of backward rupture show lower corner frequency and gentle spectral decay. As shown in Figure 3a,b, TCU071 for the 0327 event and TCU071 and CHY074 for the 0602 event exhibit both higher corner frequencies and steeper source spectral decay, indicating that the stations are located in the direction of forward rupture. In contrast, HWA033 for the 0327 event and TCU088 and HWA033 for the 0602 event show lower corner frequency and gentle spectral decay, suggesting that those stations are located in the direction of backward rupture. These observed phenomena are coincident with the rupture directions inferred by the analyses of the source time functions. In addition, Wang *et al.* (2010) noted that most events of M_L 4.4–5.5 have a corner frequency of 3–7 Hz when obtained using P-wave spectra and 2–5 Hz when obtained using S-wave spectra, which is consistent with the corner frequency of the EGF event in our case.

For the strong ground motion simulation using the EGF method, Figure 3c,d shows the average observed source spectral ratios and the fitting source spectral ratio functions for both events, and comparisons of the observed and synthetic waveforms at four stations using source spectral ratio fitting are shown in Figure 4 (comparisons of those in other stations for validation of the forward modeling are shown in Fig. 5). Most features of the observed velocity and displacement records could be well reproduced. As mentioned above, because we use the same event as the EGF, there must be a trade-off for determining the optimum parameters of both events. Additionally, inaccuracy of both the focal mechanism and attenuation effect might introduce errors into the amplitudes of synthetic waveforms. Differences in the radiation patterns between the mainshock and EGF for both the 0327 and 0602 events are also an important factor. Such differences would lead to a slight overestimation of the synthetic amplitudes for some stations (e.g., TCU088, HWA058, and HWA033). Der *et al.* (1991) noted the quality of waveform fitting varies strongly with frequency, becoming worse with increasing frequency. Indeed, the cross-correlation coefficients of the synthetic and observed waveforms for the acceleration records, which are dominated by high frequencies, are much smaller than those for the velocity and displacement records (Figs. 4 and 5).

Table 2

Parameters of Strong-Motion Generation Areas Determined by the Strong Ground Motion Simulations

	M_0 (N·m)[*]	N	C	Rupture Starting Point[†]	L (km)[‡]	W (km)[§]	V_r (km/s)	τ (s)[‖]	S (km^2)[#]	SMGA (km^2)	$\Delta\sigma_{\mathrm{SMGA}}$ (MPa)[**]	S_{ASP} (km^2)[††]	$\Delta\sigma_{\mathrm{ASP}}$ (MPa)[‡‡]
0327 event	1.17×10^{18}	3	2.22	(1, 3)	3.9	2.7	3.2	0.27	900	10.53	9.0	180	0.5
0602 event	3.28×10^{18}	4	2.55	(4, 4)	5.2	3.6	2.9	0.36	900	18.72	14.2	144	1.9

[*] Seismic moment determined by the Global Centroid Moment Tensor solution.

[†] Rupture starting point defined as initiation number of N along the strike and dip, respectively.

[‡] Length of the strong-motion generation area.

[§] Width of the strong-motion generation area.

[‖] Rise time for the mainshock.

[#] Total rupture area estimated from Chuang *et al.* (2013).

[**] Stress drop of the strong-motion generation area.

[††] Characterized asperity from Chuang *et al.* (2013) according to Somerville *et al.* (1999).

[‡‡] Stress drop of the characterized asperity.

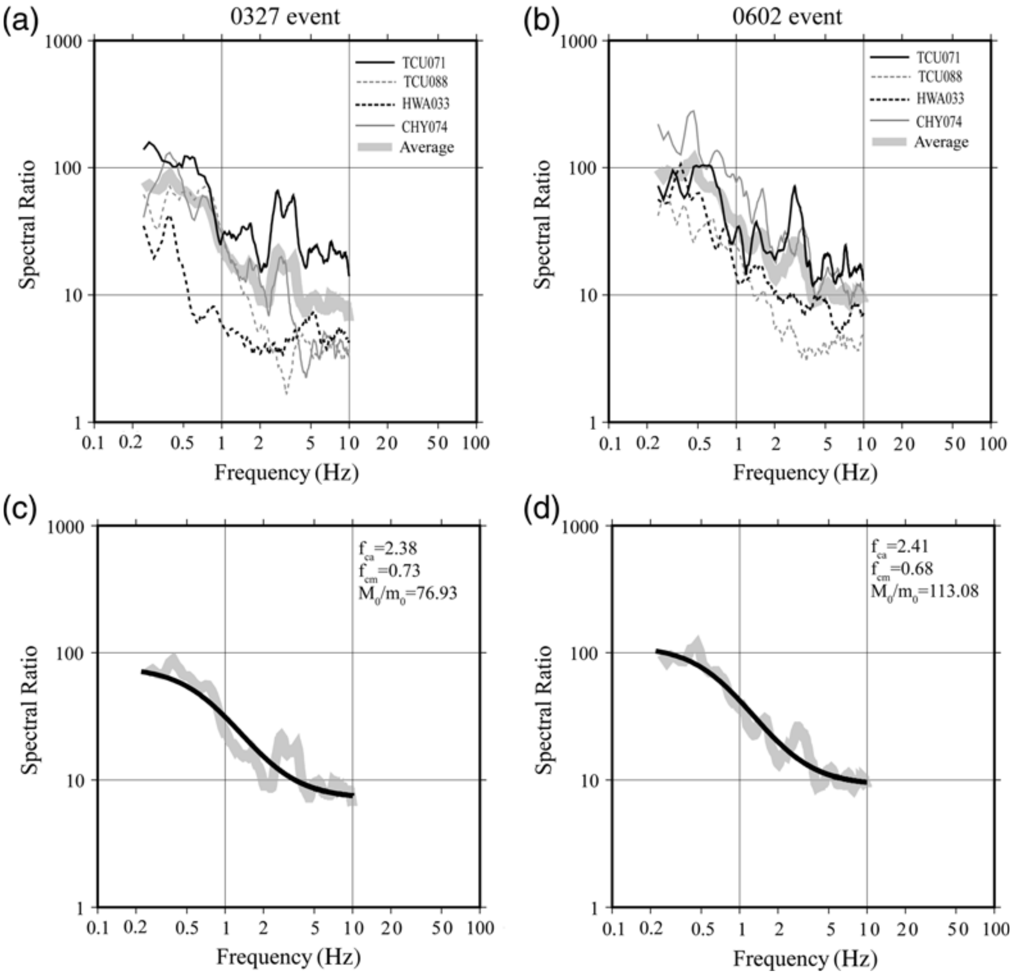

Figure 3. Source spectral ratios of the mainshock to the EGF event for the (a) 0327 and (b) 0602 events, and average observed source spectral ratios (thick gray lines) and fitting source spectral ratio function (black lines) for the (c) 0327 and (d) 0602 events, respectively. The values of the parameters determined from the source spectral ratio fitting are listed.

Considering the specific area of large slip and the overall slip area, static stress drops were evaluated using the relation among stress drop, seismic moment, and the equivalent radius of slip area. The estimated stress drops in the SMGA ($\Delta\sigma_{\mathrm{SMGA}}$) obtained from the near-field broadband seismic data were 9.0 and 14.2 MPa for the 0327 and 0602 events, respectively. Conversely, the estimated stress drops for the characterized asperity ($\Delta\sigma_{\mathrm{ASP}}$) derived by the geodetic data were 0.5 and 1.9 MPa for the 0327 and 0602 events, respectively.

Discussion and Conclusions

Our results of deconvolution analyses agree with the observed peak ground velocity data, which indicate that the 0602 event shows a clear rupture directivity effect pointing to the southwest but that the 0327 event only shows the up-dip direction of rupture directivity to the west (Fig. 2a,b). Miyake *et al.* (2001) noted that the rupture starting point in the source modeling for estimating SMGA is sensitive to the rupture directivity effect corresponding to the seismograms recorded by seismic stations at various azimuths. Because these two 2013 Nantou earthquakes were moderate-sized events, we assume that the slip direction is consistent on the fault plane during faulting. Using the focal mechanism determined by BATS (Table 1), Figure 2a,b shows a schematic of the slip direction and the rupture starting point on the SMGA for the two 2013 Nantou earthquakes. The starting points of the two 2013 Nantou earthquakes are located on the bottom of the SMGAs, which corresponds to the up-dip rupture for both events. For the 0327 event, the starting point is located on the south end of the SMGA, with a slip vector to the west; this is consistent with the minimal directivity mentioned by Aagaard *et al.* (2004). Therefore, only the up-dip direction of rupture directivity could be observed from the deconvolution analyses. Conversely, the propagation direction is more consistent with the slip direction during the faulting of the 0602 event, which satisfies the requirement of a stronger rupture directivity effect (Aagaard *et al.*, 2004). Usually, a large event with long and unilateral rupture would result in an obvious rupture directivity effect. However, the 2013 Nantou earthquakes, which were moderate-sized blind-fault events with reverse slip, resulted in noticeable rupture directivity effects and strong ground shak-

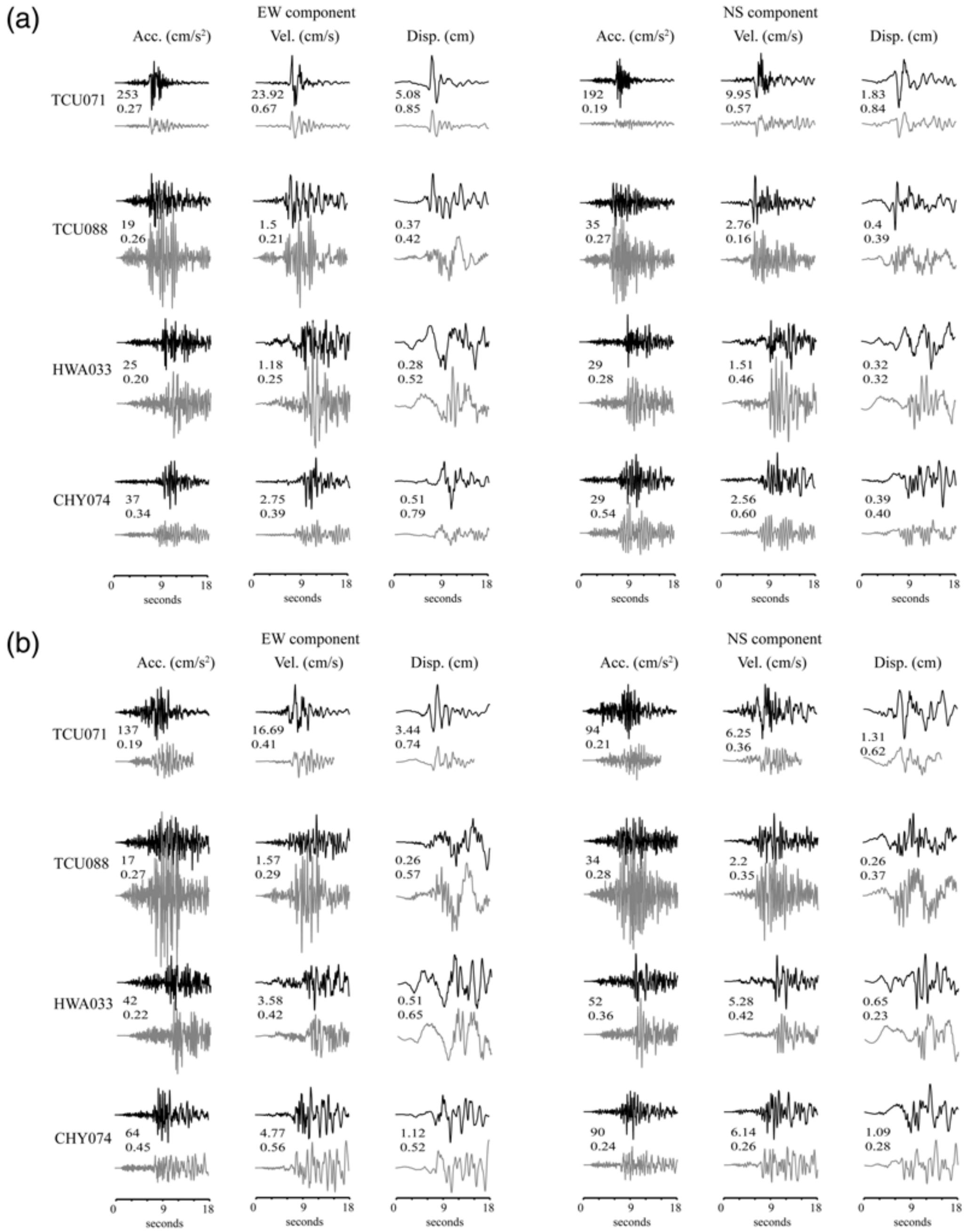

Figure 4. Comparison of observed (black lines) and synthetic (gray lines) waveforms at strong-motion stations used for the source modeling of the (a) 0327 and (b) 0602 events, with the number indicating (1) above: the maximum amplitudes of the observed records and (2) below: the cross-correlation coefficient of the synthetic and observed data.

ing. Is this a special case or a general source property of the Nantou area? More cases and further investigations are needed.

Yen and Ma (2011) investigated the source-scaling relationships of the effective fault dimensions to the seismic moment for earthquakes in Taiwan and found that most of the events had a stress drop of 1–10 MPa. Although the estimated stress drop of the 0602 event is approximately 1.5–4 times the value of the 0327 event, these values seem to be acceptable for these two crustal events. Miyake *et al.* (2001, 2003) suggested the SMGA occupied almost the same area of the characterized asperity of the waveform inversion model, and this area is about 22% of the total fault rupture area. Although we used the trimming criteria of Somerville *et al.* (1999) to estimate total fault rupture area and the characterized asperity from the inversion model of Chuang *et al.* (2013), the trimmed total rupture area is the same as the assumed fault-plane area of Chuang *et al.* (2013). This made the estimated SMGA only 1%–2% of the trimmed total rupture area for both events. On the other hand, using the empirical scaling law of Yen and Ma (2011) with the seismic moment

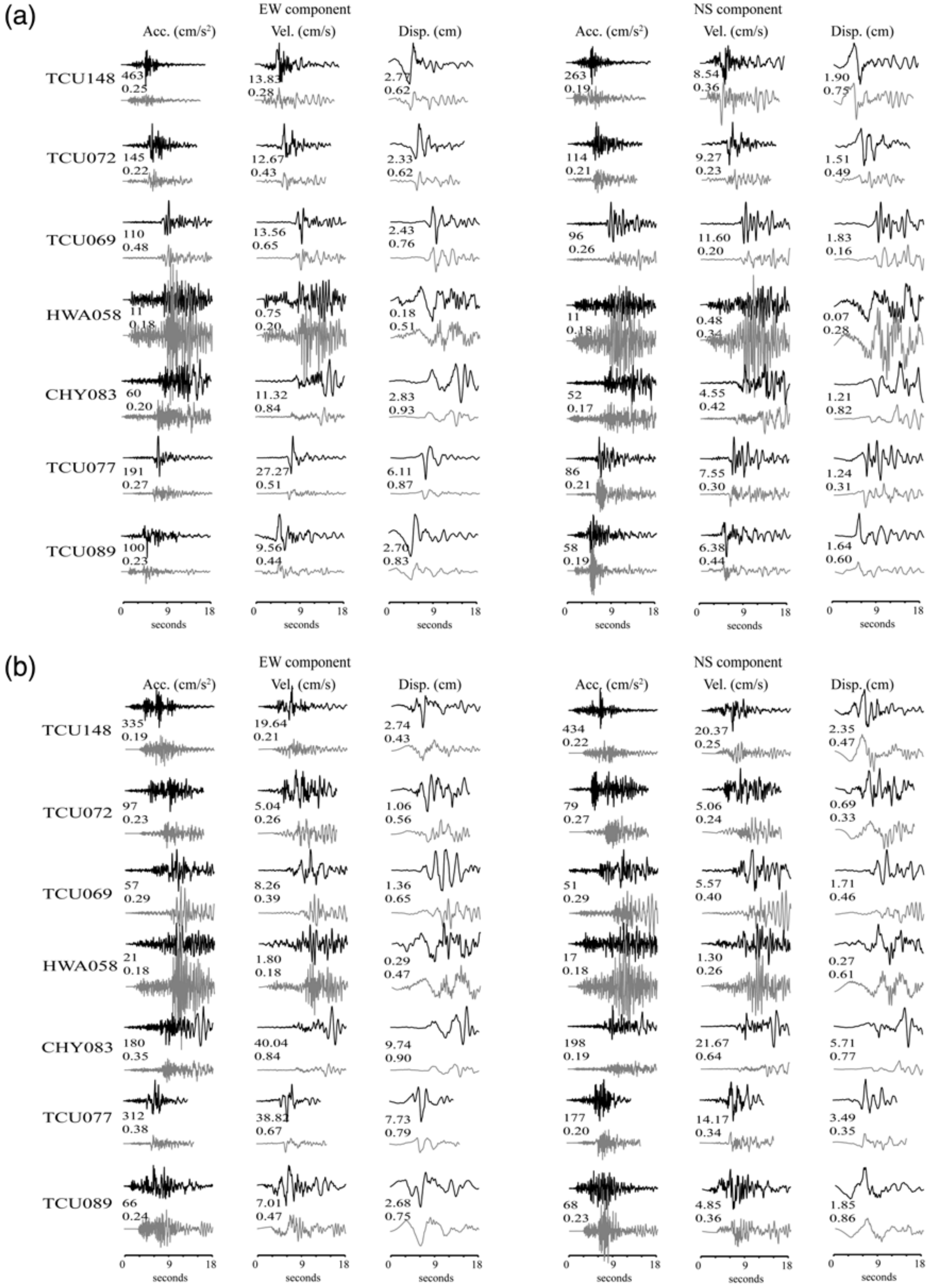

Figure 5. Comparison of observed (black lines) and synthetic (gray lines) waveforms at the strong-motion stations used for forward ground-motion simulations of the (a) 0327 and (b) 0602 events, with the number indicating (1) above: the maximum amplitudes of the observed records and (2) below: the cross-correlation coefficient of the synthetic and observed data.

obtained by the Global CMT solution to calculate the effective rupture area, we get the effective rupture area of 101 and 231 km^2 for the 0327 and 0602 events, respectively. Then, the estimated SMGA is about 10% of the effective rupture area for both events. Following the work of Miyake *et al.* (2003), we compared the scaling relationship for the seismic moment

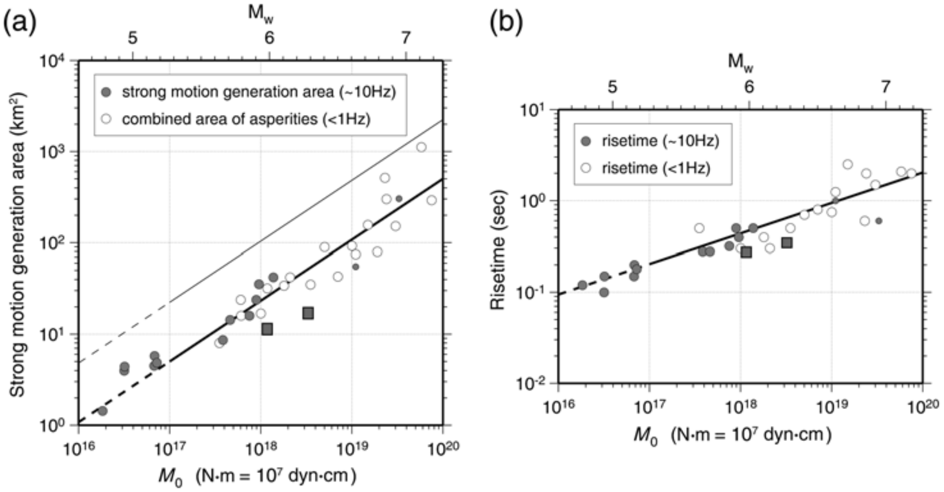

Figure 6. The scaling relationship for seismic moment versus (a) the SMGA and (b) the rise time from Miyake *et al.* (2003). Squares indicate our results for the two 2013 Nantou earthquakes superimposed on the figures.

versus the SMGA and the rise time (Fig. 6a,b). The rise time of both events agrees well with the scaling relationship; however, the SMGA seems to be smaller compared with the scale for both events. The large trimmed total rupture area (S) and characterized asperities (S_{ASP}) and small estimated stress drops ($\Delta\sigma_{\mathrm{ASP}}$) might indicate that the long-period geodetic data can only reveal a limited resolution of the source properties. Another possible interpretation is that the estimated stress drop for the SMGA and the characterized asperities may correspond to dynamic and static stress drops, respectively. The slip model derived from higher resolution data, such as seismic waveform data, is needed for further investigation and analysis.

Manighetti *et al.* (2007) showed that the earthquake stress drop strongly relates to the structural maturity of the ruptured fault, and Radiguet *et al.* (2009) concluded that both an immature fault and a blind fault would enhance the strong ground motions. Chuang *et al.* (2013) suggested the two 2013 Nantou earthquakes nucleated on essentially the same ramp fault, which might be a newly developed deep subsurface structure and has no direct relation with any faults at the surface. These two events, which occurred within such a short distance, show large differences in their rupture properties and stress drop; this indicates the possibility of striking stress heterogeneity on this ramp fault. However, exploring such a mechanism of variability would require additional data and is beyond the scope of this study. Yen and Ma (2011) pointed out that the significant high stress-drop events yield locally high peak ground acceleration. Other recent studies also noted the importance of variability of stress drop and apparent stress (e.g., Baltay *et al.*, 2011; Oth, 2013). Therefore, more study is required to better investigate both the nature of localized high peak ground acceleration and seismic hazard associated with future earthquakes around this area.

The results show that from combining the deconvolution analysis and strong ground motion simulation, the 0327 event only shows the up-dip direction of rupture directivity; however, the significant directivity effect of the 0602 event, with the rupture propagating to the southwest, is identified. Except for the rupture behavior, the obvious differences in the stress drop of these two nearby events highlight the stress heterogeneity and potential of seismic hazard in this region. Our study shows the integrated analysis using EGF methods provides more comprehensive information to better understand earthquake source properties and the potential impact to seismic-hazard assessment. Because seismicity is extremely active in Taiwan, it is important to analyze more cases, especially for the moderate-sized events originating from the buried faults, for the mitigation of any future seismic hazards.

Data and Resources

All data used in this paper came from published sources listed in the references, and all figures were generated using the Generic Mapping Tools version 4.3.1 (www.soest.hawaii.edu/gmt/; last accessed August 2014; Wessel and Smith, 1998).

Acknowledgments

We thank Associate Editor Michel Bouchon and an anonymous reviewer for their helpful comments. We thank the Central Weather Bureau (CWB) of Taiwan and Broadband Array in Taiwan for Seismology (BATS) for providing high-quality seismic data. This research was supported by the Taiwan Earthquake Center (TEC) and funded through the National Science Council (NSC), Taiwan, with Grant Number NSC102-2116-M-194-013. The TEC contribution number for this article is 00110.

References

Aagaard, B. T., J. F. Hall, and T. H. Heaton (2004). Effects of fault dip and slip rake angles on near-source ground motions: Why rupture directivity was minimal in the 1999 Chi-Chi, Taiwan, earthquake, *Bull. Seismol. Soc. Am.* **94,** 155–170.

Ammon, J. C., C. Ji, H. Thio, D. Robinson, S. Ni, V. Hjorleifsdottir, H. Kanamori, T. Lay, S. Das, D. Helmberger, G. Ichinose, J. Polet, and D. Wald (2005). Rupture process of the 2004 Sumatra–Andaman earthquake, *Science* **308,** 1133–1139.

Baltay, A., S. Ide, G. Prieto, and G. Beroza (2011). Variability in earthquake stress drop and apparent stress, *Geophys. Res. Lett.* **38,** L06303, doi: 10.1029/2011GL046698.

Boatwright, J. (1988). The seismic radiation from composite models of faulting, *Bull. Seismol. Soc. Am.* **78,** 489–508.

Boore, D. M., and W. B. Joyner (1978). The influence of rupture incoherence on seismic directivity, *Bull. Seismol. Soc. Am.* **68,** 283–300.

Brune, J. N. (1970). Tectonic stress and the spectra of seismic shear waves from earthquakes, *J. Geophys. Res.* **75,** 4997–5009.

Brune, J. N. (1971). Correction, *J. Geophys. Res.* **76,** 5002.

Carena, S., J. Suppe, and H. Kao (2002). Active detachment of Taiwan illuminated by small earthquakes and its control of first-order topography, *Geology* **30,** 935–938.

Central Geological Survey (2013a). Geological survey report for the 20130327 Nantou earthquake, Center Geol. Surv. MOEA, ROC, http://fault.moeacgs.gov.tw/TaiwanFaults_2009/PageContent.aspx?type=C&id=246 (last accessed October 2014) (in Chinese)

Central Geological Survey (2013b). Geological survey report for the 20130602 Nantou earthquake, Center Geol. Surv. MOEA, ROC, http://fault.moeacgs.gov.tw/TaiwanFaults_2009/PageContent.aspx?type=C&id=247 (last accessed October 2014) (in Chinese).

Cheng, S.-N., Y. T. Yeh, M.-T. Hsu, and T.-C. Shin (1999). *Photo Album of Ten Disastrous Earthquakes in Taiwan, Central Weather Bureau and Institute of Earth Science*, Academia Sinica, Taipei, Taiwan (in Chinese).

Chu, R., L. Zhu, and D. V. Helmberger (2009). Determination of earthquake focal depths and source time functions in central Asia using teleseismic P waveforms, *Geophys. Res. Lett.* **36,** L17317, doi: 10.1029/2009GL039494.

Chuang, R. Y., K. M. Johnson, Y.-M. Wu, K.-E. Ching, and L.-C. Kuo (2013). A midcrustal ramp-fault structure beneath the Taiwan tectonic wedge illuminated by the 2013 Nantou earthquake series, *Geophys. Res. Lett.* **40,** 5080–5084, doi: 10.1002/grl.51005.

Der, Z. A., R. H. Shumway, and M. R. Hirano (1991). Time domain waveform inversion—A frequency domain view: How well we need to match waveforms? *Bull. Seismol. Soc. Am.* **81,** 2351–2370.

Irikura, K. (1986). Prediction of strong acceleration motions using empirical Green's function, in *Proc. 7th Japan Earthquake Engineering Symposium*, Tokyo, Japan, 10–12 December 1986, 151–156.

Irikura, K., and K. Kamae (1994). Estimation of strong ground motion in broad-frequency band based on a seismic source scaling model and an empirical Green's function technique, *Ann. Geofisc.* **37,** 1721–1743.

Kikuchi, M., and H. Kanamori (1982). Inversion of complex body waves, *Bull. Seismol. Soc. Am.* **72,** 491–506.

Kuo-Chen, H., F. T. Wu, and S. W. Roecker (2012). Three-dimensional P velocity structures of the lithosphere beneath Taiwan from the analysis of TAIGER and related seismic data sets, *J. Geophys. Res.* **117,** no. B06306, doi: 10.1029/2011JB009108.

Lay, T., and T. C. Wallace (1995). *Modern Global Seismology*, Academic Press, San Diego, California.

Madariaga, R. (1979). On the relation between seismic moment and stress drop in the presence of stress and strength heterogeneity, *J. Geophys. Res.* **84,** 2243–2250.

Manighetti, I., M. Campillo, S. Bouley, and F. Cotton (2007). Earthquake scaling, fault segmentation, and structural maturity, *Earth Planet. Sci. Lett.* **253,** 429–438.

Miyake, H., T. Iwata, and K. Irikura (1999). Strong ground motion simulation and source modeling of the Kagoshima-ken Hokuseibu earthquakes of March 26 (M_{JMA} 6.5) and May 13 (M_{JMA} 6.3), 1997, using empirical Green's function method, *Zisin* **51,** 431–442 (in Japanese with English abstract).

Miyake, H., T. Iwata, and K. Irikura (2001). Estimation of rupture propagation direction and strong motion generation area from azimuth and distance dependence of source amplitude spectra, *Geophys. Res. Lett.* **28,** 2727–2730.

Miyake, H., T. Iwata, and K. Irikura (2003). Source characterization for broadband ground-motion simulation: Kinematic heterogeneous source model and strong motion generation area, *Bull. Seismol. Soc. Am.* **93,** 2531–2545.

Orefice, A., M. Vallée, J. Balestra, B. Delouis, and A. Zollo (2013). Refined rupture-velocity estimation of the 2009 L'Aquila earthquake (M_{w} 6.3, Central Italy) derived from apparent source time functions, *Bull. Seismol. Soc. Am.* **103,** 2474–2481.

Oth, A. (2013). On the characteristics of earthquake stress release variations in Japan, *Earth Planet. Sci. Lett.* **377/378,** 132–141.

Radiguet, M., F. Cotton, I. Manighetti, M. Campillo, and J. Douglas (2009). Dependency of near-field ground motions on the structural maturity of the ruptured faults, *Bull. Seismol. Soc. Am.* **99,** 2572–2581.

Somerville, P., K. Irikura, R. Graves, S. Sawada, D. Wald, N. Abrahamson, Y. Iwasaki, T. Kagawa, N. Smith, and A. Kowada (1999). Characterizing crustal earthquake slip models for the prediction of strong ground motion, *Seismol. Res. Lett.* **70,** 59–80.

Velasco, A. A., C. J. Ammon, and T. Lay (1994). Empirical Green function deconvolution of broadband surface waves: Rupture directivity of the 1992 Landers, California ($M_{\mathrm{w}} = 7.3$) earthquake, *Bull. Seismol. Soc. Am.* **84,** 735–750.

Wang, Y.-J., K.-F. Ma, F. Mouthereau, and D. Eberhart-Phillips (2010). Three dimensional Q_P- and Q_S-tomography beneath Taiwan Orogenic Belt: Implication for tectonic and thermal structure, *Geophys. J. Int.* **180,** 891–910.

Wen, Y.-Y., K.-F. Ma, and D. D. Oglesby (2012). Variations in rupture speed, slip amplitude, and slip direction during the 2008 M_{w} 7.9 Wenchuan earthquake, *Geophys. J. Int.* **190,** 379–390.

Wessel, P., and W. H. F. Smith (1998). New, improved version of generic mapping tools released, *EOS Trans. AGU* **79,** 579.

Wu, F. T., C. S. Chang, and Y. M. Wu (2004). Precisely relocated hypocenters, focal mechanisms and active orogeny in Central Taiwan, in *Aspects of the Tectonic Evolution of China*, special publications, J. Malpas, C. J. N. Fletcher, J. R. Ali, and J. C. Aitchison (Editors), Vol. 226, Geol. Soc., London, United Kingdom, 333–354.

Yen, Y.-T., and K.-F. Ma (2011). Source-scaling relationship for M 4.6–8.9 earthquakes, specifically for earthquakes in the collision zone of Taiwan, *Bull. Seismol. Soc. Am.* **101,** 464–481.

Yue, L. F., J. Suppe, and J. H. Hung (2005). Structural geology of a classic thrust belt earthquake: The 00201999 Chi-Chi earthquake Taiwan ($M_{\mathrm{w}} = 7.6$), *J. Struct. Geol.* **27,** 2058–2083.

Department of Earth and Environmental Sciences
National Chung-Cheng University
Chia-Yi County 62102, Taiwan
yiyingwen@ccu.edu.tw
(Y.-Y.W.)

Earthquake Research Institute
University of Tokyo
Tokyo 113-0032, Japan
(H.M.)

Sinotech Engineering Consultants, Inc.
Taipei 11494, Taiwan
(Y.-T.Y.)

Disaster Prevention Research Center
Aichi Institute of Technology
1247 Yachigusa, Yakusa-cho, Toyota
Aichi 470-0392, Japan
(K.I.)

Department of Geomatics
National Cheng Kung University
Tainan 70101, Taiwan
(K.-E.C.)

Manuscript received 17 April 2014;
Published Online 28 October 2014